

Exploring the role of accretion shocks in galaxy clusters as sources of ultrahigh-energy cosmic rays

A.D. Supanitsky*

*Instituto de Tecnologías en Detección y Astropartículas (ITeDA,
CNEA-CONICET-UNSAM),
Centro Atómico Constituyentes, PC 1650,
San Martín, Buenos Aires, Argentina*

S.E. Nuza†

*Instituto de Astronomía y Física del Espacio (IAFE,
CONICET-UBA), PC 1428 Buenos Aires, Argentina
(Dated: January 27, 2026)*

Recently, the Pierre Auger Observatory has found strong evidence supporting the extragalactic origin of the most energetic cosmic rays. Despite several observed excesses in the distribution of arrival directions for the highest energy cosmic rays, the sources remain unidentified. Accretion shocks in galaxy clusters have been proposed as potential sources in the past. These immense shock waves, which can have radii on the order of megaparsecs, are generated by the infall of material from the intergalactic medium into the gravitational potential wells of galaxy clusters. In this work, we investigate the possibility that ultrahigh-energy cosmic rays are accelerated in these regions. Nearby massive galaxy clusters, including Virgo, are treated as a discrete component of the cluster mass distribution. Less massive galaxy clusters, as well as distant massive ones, are assumed to follow a continuous distribution in agreement with cluster mass statistics. We fit the flux at Earth and the composition profile measured by the Pierre Auger Observatory, assuming the injection of different nuclear species by these sources, to determine the values of the model parameters. Our results indicate that cosmic ray acceleration in cluster accretion shocks may account for at least a fraction of the observed UHECR flux at energies below the suppression scale. At higher energies, direct acceleration from the thermal pool would be feasible only if local fluctuations create favorable conditions, such as magnetic fields about an order of magnitude stronger than those typically expected in cluster accretion shocks, or for particular shock normal-magnetic field configurations. Moreover, in these scenarios, where the energy spectrum of accelerated cosmic rays is modeled as $\propto E^{-\gamma}$ with an exponential cutoff, the spectral index obtained from fitting the experimental data lies in the range $\gamma \sim 0.7 - 1.6$. This is smaller than 2, which is the value expected from the first-order Fermi acceleration mechanism for strong shocks.

I. INTRODUCTION

The origin of ultrahigh-energy cosmic rays (UHECRs, $E \geq 10^{18}$ eV) remains an open question in high-energy astrophysics. However, the vast amount of data collected by current observatories has led to the discovery of several key features of these highly energetic particles, which are crucial for understanding their nature. The observatories currently in operation include the Pierre Auger Observatory (Auger) [1] in the southern hemisphere and Telescope Array (TA) [2] in the northern hemisphere, Auger being the bigger one covering an area of $\sim 3,000$ km².

The energy spectrum of the UHECRs has been measured with great accuracy, thanks to the large exposure accumulated, particularly by Auger. Several distinctive features are observed: a hardening at approximately 5×10^{18} eV, known as the ankle, a steepening at around

10^{19} eV referred to as the instep; and a sharp drop at approximately 5×10^{19} eV known as the suppression [3, 4]. Although there are various models explaining the origin of these features, they remain the subject of ongoing debate.

The composition of the UHECRs is inferred mainly from the atmospheric depth of the shower maximum, X_{\max} , a parameter very sensitive to the primary mass together with the muon content of the showers [5]. X_{\max} is measured with the fluorescence telescopes, which take data on clear and moonless nights. Therefore, the duty cycle is smaller compared to that of the surface detectors, reducing the statistics of events with available X_{\max} by approximately a factor of 10. Composition analyses rely on comparing experimental data with simulations of atmospheric air showers. Since the high-energy hadronic interactions at ultrahigh energies are not fully understood, air shower simulations use models that extrapolate low-energy accelerator data to these higher energies. This approach introduces non-negligible systematic uncertainties in the composition determination. Despite these challenges, the Auger X_{\max} data indicate that the composition appears to become progressively lighter from

* daniel.supanitsky@iteda.gob.ar

† snuza@iafe.uba.ar

energies below 10^{18} eV up to around $10^{18.3}$ eV, where a change in composition occurs [6, 7]. Above this energy, the composition seems to become increasingly heavier. Additionally, the variance of X_{\max} suggests that the composition is becoming purer as the energy increases. Recently, Auger significantly increased the statistics of X_{\max} data by approximately a factor of 10 after incorporating surface detector measurements in the analysis [8, 9]. This enhanced dataset reveals evidence of three distinct breaks in the mean value of X_{\max} as a function of the logarithm of energy. These features are observed near the ankle, the instep, and the suppression regions. Furthermore, the transition toward a heavier primary composition is confirmed up to the suppression region, a result made possible by the substantial improvement in statistics.

Regarding the distribution of the arrival directions, Auger has measured a dipolar anisotropy above 8×10^{18} eV [10, 11]. The amplitude of the dipole is approximately 7.3%, with the significance of the measurements reaching 6.9σ . One of the most important implications of this finding is that a galactic origin of the UHECRs seems to be very unlikely. At small and intermediate angular scales several excesses have been found by both, Auger and TA observatories. In the case of Auger, the data show an excess in the region of the radio galaxy Centaurus A but the significance of this excess is at the level of 4σ [10]. Similarly, data from the TA observatory show two excesses [12]. The first is known as the hotspot, and it is located near the Ursa Major constellation, with the excess showing a significance level of 2.8σ . The second one is located in the region of Perseus-Pisces supercluster, with the excess showing a significance of 3.3σ . It is worth mentioning that Auger analyzed these two sky regions with comparable statistics and found no significant signal, indicating that more studies have to be performed to understand this tension. Moreover, Auger data also reveal an excess in the directions of several nearby starburst galaxies, with a significance of 3.8σ [10]. Therefore, despite the great effort made, the sources of UHECRs have not yet been identified.

The origin of the ankle remains unclear, and two main models have been proposed to explain it. The first suggests the existence of two populations of sources: one responsible for the lighter cosmic rays (CRs) below the ankle, and the other, consisting of intermediate and possibly heavy nuclear species, becoming significant at energies above the ankle [13–15]. In the second scenario, the light component below the ankle is produced by the photodisintegration of high-energy heavy nuclei in the photon field of the sources or their environment [16–21]. The origin of the instep and the suppression are still being investigated. These two features appear to result from the exponential cutoff of the injected spectrum, modified by the propagation of the helium and nitrogen components in the intergalactic medium, respectively [15].

Accretion shocks in galaxy clusters have also been suggested as potential sources of UHECRs [22–27]. These gi-

ant accretion shock waves can span several megaparsecs in radius and are capable of accelerating particles to the highest energies. They are generated by the infall of material from the intergalactic medium onto the high-density cluster regions within the cosmic web. In Ref. [22], UHECRs from galaxy cluster accretion shocks are modeled considering only protons for their composition, in line with expectations before the advent of Auger. However, both observations and cosmological simulations suggest the presence of metals in galaxy cluster outskirts (see e.g. Ref. [28]). In Ref. [23], heavier nuclei are also considered assuming a continuous distribution of sources, which fails to properly account for the contribution of nearby sources, an important factor in this case, especially due to the presence of the Virgo supercluster. In Ref. [24], only the contribution of the Virgo cluster is studied, without considering other nearby or more distant galaxy clusters. Finally, in Refs. [25, 26], the authors discuss the possibility that UHECRs are accelerated in galaxy cluster accretion shocks without fitting the measured energy spectrum and composition profile. In particular, in Refs. [26, 27], a hierarchical model in which CRs of all energies are explained through the action of the diffusive shock acceleration (DSA) mechanism across progressively larger scales is proposed. In this scenario, a high-energy population of CRs accelerated in the termination shocks of powerful galaxies can undergo further acceleration in the accretion shocks of galaxy clusters, leading to the UHECR component.

In this work, we develop a model for the highest-energy component of UHECRs (the one above the ankle), where these extremely energetic particles are accelerated in the accretion shocks of galaxy clusters. The model assumes that the sources inject a mixture of nuclear species, including light, intermediate, and heavy nuclei. We assume that CRs are accelerated via the first-order Fermi mechanism. To estimate two key parameters required by DSA, i.e. the magnetic field in the acceleration region and the velocity of the shock waves, we use two different approaches: the first is based on simplified physical considerations, while the second additionally relies on cosmological simulations. The contribution of nearby massive galaxy clusters is taken into account considering a discrete set of nearby sources, including Virgo. The contribution of less massive galaxy clusters in our vicinity, and of more distant ones, are also included in our model assuming a continuous distribution of sources following the universal halo mass function determined from cosmological simulations. We determine model parameters by fitting the Auger spectrum and composition profile and, based on the results of this fit, discuss the possibility that accretion shocks in galaxy clusters are responsible for the observed UHECRs.

This article is organized as follows. In Sec. II, we describe the model for the injected spectrum of the sources including the estimation of the magnetic field in the outskirts of galaxy clusters, the velocity of the infalling shock waves and the maximum energy attained by the CRs,

which is obtained from the acceleration and interaction times of particles in the acceleration region. Also included in this section is a description of the discrete sample of local clusters considered. In Sec. III, we present the method used to calculate the different contributions to the spectrum and composition profile, which is based on the simulation of the propagation of CRs in the intergalactic medium from the acceleration site to the observer. We also describe the fit procedure and the results obtained. In Sec. IV, we discuss our results. Finally, in Sec. V, we present our conclusions.

Throughout this paper, we adopt a set of cosmological parameters consistent with the Planck cosmology given by Ref. [29]. Specifically, we assume a total matter density of $\Omega_M = 0.315$, a cosmological constant density of $\Omega_\Lambda = 0.685$, and a reduced Hubble constant of $h = 0.673$.

II. INJECTED SPECTRUM

A. Cosmic ray accelerators

In this section, CR acceleration within large-scale accretion shocks developed in the external regions of galaxy clusters is modeled. CR protons and nuclei are assumed to gain energy by multiple shock crossings until they escape the accelerator region to further propagate through the intergalactic medium. These locations are therefore considered as plausible sites for CR acceleration that may be responsible for, at least, some of the UHECR observed population. One key ingredient in the modeling of accretion shocks is the galaxy cluster mass. Since the total gravitating mass of a system is better represented by the so-called *virial* mass, M_{vir} (i.e., the total mass within the virial radius, R_{vir}), virial quantities will be used to characterize galaxy clusters, unless stated otherwise. The virial radius corresponds to the distance from the center of the cluster for which the enclosing mean mass density is equal to the virial density contrast, Δ_{vir} , times the critical density of the Universe, where $\Delta_{\text{vir}} = \Delta_{\text{vir}}(\Omega_i, z)$ depends both on cosmology and redshift [30]. In the following, the main ingredients of the model concerning magnetic fields and shocked gas velocities at the acceleration sites are presented.

1. Magnetic fields at cluster outskirts

The magnetic field B at the location of accretion shocks is computed assuming that the thermal pressure of the gas is proportional to the magnetic energy density. Therefore,

$$\frac{B^2}{8\pi} = \beta^{-1} \frac{\rho}{\mu m_p} kT, \quad (1)$$

where β is the plasma beta parameter, ρ and T are the gas density and temperature in the shock region, k is the

Boltzmann constant, μ is the mean molecular weight and m_p is the proton mass. Solving for the magnetic field the following expression is obtained

$$B(P) = 200 \mu\text{G} \times \sqrt{\beta^{-1} P \text{keV}^{-1} \text{cm}^3}. \quad (2)$$

In this equation, P is the gas pressure at the distance of the accretion shock. In this way, the magnetic field strength can be directly related to the gas pressure, thereby encapsulating the dependence on cluster mass and redshift through the pressure at the acceleration site. To account for the latter in galaxy clusters, the validity of the universal pressure profile determined in Ref. [31] is assumed, based on the REXCESS survey [32], a representative sample of 33 local galaxy clusters up to $z = 0.2$. This function parametrizes the gas pressure profile for radial distances from the cluster center at $0.03 \leq r/R_{500} \leq 4$, where R_{500} is the radius enclosing a mass density 500 times the critical density of the Universe, as a function of $M_{500} \equiv M_{\text{tot}}(r \leq R_{500})$ and redshift z . Since the cluster virial radius is $R_{\text{vir}} \sim 2R_{500}$, this profile is thus generally valid at cluster outskirts, at least out to $r \sim 2R_{\text{vir}}$. This is important because accretion shocks surrounding massive galaxy clusters can be formed in the cluster outskirts, up to a distance of a few times the virial radius, as shown, for instance, in Ref. [33].

Once the ambient gas pressure, P_1 , at the location of external shocks is computed using the universal pressure profile from Ref. [31], the pressure in the downstream region, P_2 , can be determined using the Rankine-Hugoniot conditions for hydrodynamical shocks. The pressure jump between the pre- and postshock regions is (e.g. Ref. [34])

$$\frac{P_1}{P_2} = \frac{(\gamma_a + 1) - (\gamma_a - 1)\chi}{(\gamma_a + 1)\chi - (\gamma_a - 1)}, \quad (3)$$

where χ is the compression ratio that depends on the shock Mach number \mathcal{M} and γ_a is the adiabatic index. To compute the pressure jump in the accretion shocks, it is necessary to provide their Mach number. One possibility is to estimate its value based on an approximation for the infall shock velocity and the local sound speed of the intracluster medium. However, to avoid making assumptions about arbitrary shock velocities, the Mach number *stacked* profile, $\mathcal{M}(r)$, of the material surrounding massive galaxy clusters is directly employed, as provided by the cosmological simulations of Ref. [33] (see, e.g., their Fig. 6), where typical average Mach number values at these locations are approximately $\mathcal{M} \gtrsim 10$. Therefore, by computing $B_2 \equiv B(P_2)$ in Eq. (2) it is possible to obtain a magnetic field estimate in the shock region.

As shown in Ref. [35], accretion shocks in the outskirts of galaxy clusters exhibit a plasma beta parameter of $\beta \gtrsim 100$. This is in contrast with the case of internal shocks which typically display lower values. In the calculations below, a value of $\beta = 100$ is assumed, unless otherwise stated. This yields magnitudes below the μG level in agreement with expectations from numerical simulations.

2. Accretion shock velocity

The material falling onto the cluster potential wells get accelerated to a terminal velocity v_{sh} . The infall velocity of noncollisional particles onto a galaxy cluster of mass M_{vir} at a distance r_{sh} from its center is

$$v_{\text{sh,in}}(r_{\text{sh}}) = \sqrt{\frac{2GM_{\text{vir}}}{r_{\text{sh}}}}, \quad (4)$$

where G is Newton's gravitational constant. Since external shocks in galaxy clusters are usually generated at distances of $r_{\text{sh}} \gtrsim R_{\text{vir}}$, the infall shock velocity follows a virial mass scaling of $v_{\text{sh,in}} \propto M_{\text{vir}}^{1/3}$.

This approximation, however, does not take into account the hydrodynamical nature of the infalling gas. Therefore, an additional estimate, dubbed $v_{\text{sh,sim}}$, is performed by adopting the universal cluster temperature profile, $T(r)$, given in Ref. [36] as a function of cluster virial temperature, T_{vir} , to get a measure of the sound speed of the intracluster medium as a function of cluster radius. By combining the radial function of the sound speed with the mass-dependent Mach number profile of Ref. [33], shock velocities in the external cluster regions are computed using the definition of Mach number, namely

$$v_{\text{sh,sim}}(r_{\text{sh}}) = \mathcal{M}(r_{\text{sh}})c_s(r_{\text{sh}}), \quad (5)$$

where $\mathcal{M}(r_{\text{sh}})$ and $c_s(r_{\text{sh}})$ are the assumed Mach number average profile and the sound speed, respectively, evaluated at the location of the shock front.

B. Accretion shock models

The approximations discussed in the previous section allow for the assumption of plausible astrophysical scenarios for accretion shocks in galaxy clusters, based on their behavior in the $B - v_{\text{sh}}$ plane, which will be used to calculate the maximum cosmic-ray acceleration velocities in Sec. II C. In this paper, four different physically motivated models for the magnetic field and infall shock velocity scalings as a function of cluster virial mass and redshift are considered. In the first scenario (model A), scalings are built from an array of cluster masses using the infall shock velocity given by Eq. (4) and the magnetic field B_2 evaluated at the virial radius. In the second scenario (model B), model A is modified replacing the infall shock velocity by that of Eq. (5), which has been motivated using cosmological simulations, leaving the magnetic field scaling unchanged. In the third scenario (model C), scalings are computed using both Eq. (5) for the shock velocity and B_2 for the magnetic field but, in this case, interpolating the simulated Mach number profile of Ref. [33] at the mean distance from the cluster center, which corresponds to about $2.5 R_{\text{vir}}$. Finally, the fourth scenario (model D), postulates a constant magnetic field of $1 \mu\text{G}$ (i.e., independent of cluster

TABLE I. Astrophysical scenarios for galaxy cluster accretion shocks assuming $\beta = 100$ (except model D which assumes a constant magnetic field). Different columns show the scaling parameters of the magnetic field (columns 2, 4, 6) and shock velocity (columns 3, 5, 7) with cluster virial mass and redshift for four different models (see text). Scalings are of the form: $\mathcal{A}_i(M_{\text{vir}}/10^{14} \text{ M}_\odot)^{\alpha_i} \times \mathcal{E}(z)^{\beta_i}$, where $i = \{\text{sh, mag}\}$ stands for the shock velocity and magnetic field cases, respectively, and $\mathcal{E}(z) = \sqrt{\Omega_M(1+z)^3 + \Omega_\Lambda}$.

Model	\mathcal{A}_{mag} [μG]	\mathcal{A}_{sh} [km s^{-1}]	α_{mag}	α_{sh}	β_{mag}	β_{sh}
A	0.145	838	0.31	1/3	4/3	0
B	0.145	688	0.31	1/3	4/3	0
C	0.068	1316	0.31	1/3	4/3	0
D	1	1316	0	1/3	4/3	0

mass) using the accretion shock velocity–mass scaling of model C. For all models, the magnetic field evolution with redshift follows from the pressure profile which, in turn, depends on cosmology. The scalings obtained for the four different models are presented in Table I.

C. Maximum energy

Following Ref. [22] it is assumed that the CRs are accelerated at the shock fronts through the first-order Fermi mechanism. Assuming that the diffusion coefficient of accretion shocks in galaxy clusters is proportional to the Bohm diffusion one, the following expression for the mean acceleration time is obtained [37]

$$\tau_{\text{acc}}(E) = \frac{\chi}{\chi - 1} \left(\frac{c}{v_{\text{sh}}} \right)^2 \frac{r_g(E)}{c} \eta \mathcal{J}(\theta, \chi, \eta), \quad (6)$$

where r_g the gyroradius, θ is the angle between the magnetic field and the shock normal, η is the proportionality constant between the diffusion coefficient parallel to the magnetic field and the Bohm diffusion coefficient, and

$$\mathcal{J}(\theta, \chi, \eta) = \cos^2 \theta + \frac{\sin^2 \theta}{1 + \eta^2} + \chi \frac{\cos^2 \theta + \chi^2 \frac{\sin^2 \theta}{1 + \eta^2}}{[\cos^2 \theta + \chi^2 \sin^2 \theta]^{3/2}}. \quad (7)$$

A compression ratio $\chi = 4$ is assumed, which corresponds to the case of a strong shock. Since, appropriate values of η are in the [1, 10] interval [38], the values $\eta = 1$ and $\eta = 10$ are considered in the subsequent calculations. Recent findings indicate that, in addition to parallel shocks, CRs might also be efficiently accelerated in quasiperpendicular shocks [39]. Therefore, the values of θ considered in this work are: 0° , 45° , and 90° .

The CRs accelerated in galaxy cluster shocks lose energy mainly due to their interactions with the low-energy photons of the cosmic microwave background (CMB) and the extragalactic background light (EBL). Therefore, the maximum energy achieved by a CR accelerated in an accretion shock corresponding to a galaxy cluster of a given

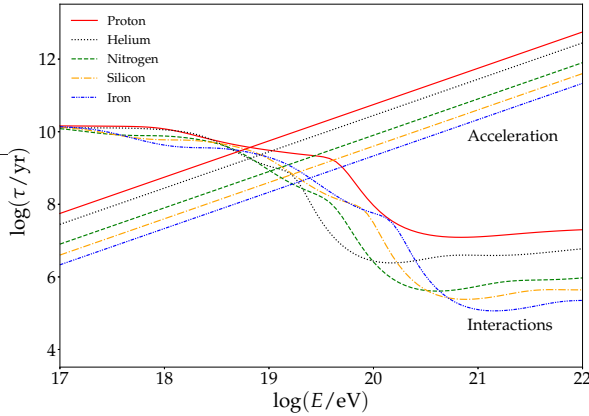


FIG. 1. Mean interaction and acceleration times as a function of the logarithm of primary energy for model C, $\eta = 1$, $\theta = 45^\circ$, and $\beta = 100$ for all nuclear species considered.

mass M_{vir} and redshift z is estimated by solving the following equation

$$\tau_{\text{int}}(E_{\text{max}}, z, Z) = \tau_{\text{acc}}(E_{\text{max}}, Z, M_{\text{vir}}), \quad (8)$$

where τ_{int} is the total mean interaction time and Z is the charge number of the nuclear species under consideration. Figure 1 shows the mean interaction time of the five nuclear species considered in this work: proton, helium, nitrogen, silicon, and iron at $z = 0$ as a function of the logarithm of the energy, obtained from CRPropa [40]. The mean interaction time shown in the figure includes the photo-pion production, photodisintegration, and pair production processes (see Appendix A for details). The energy loss due to the adiabatic expansion of the Universe is also included but its effect on the maximum energy calculation is small. The EBL model used in the mean free path calculation is the one of Ref. [41]. The figure also shows the acceleration time obtained from Eq. (6) for the five nuclear species considered in accretion model C and the quasiparallel case, $\theta = 45^\circ$, for a cluster of $10^{15} M_\odot$. From the figure it can be seen that the maximum energy for the different nuclear types ranges from $\sim 10^{18.8}$ to $\sim 10^{19.4}$ eV. The maximum energy attained by the different CR types depends on the cluster virial mass and redshift. Figure 2 shows the maximum energy corresponding to proton and iron primaries as a function of the redshift for different values of the cluster virial mass. The figure shows that the maximum energy varies more significantly with the cluster virial mass than with redshift. For any given redshift, the maximum energy can vary more than an order of magnitude for the different clusters, in contrast to the smaller variation observed at a fixed cluster mass during the redshift interval considered.

D. Cosmic ray luminosity

The differential number of CRs of mass number A injected by the sources per unit of time and energy is mod-

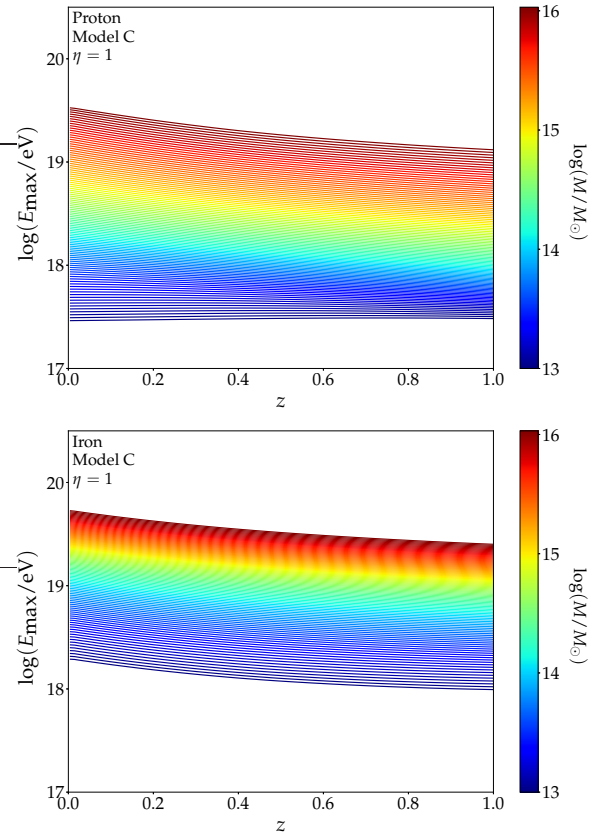


FIG. 2. Maximum energy as a function of the cluster redshift for different values of the cluster virial mass, for accretion shock model C, $\eta = 1$, $\theta = 45^\circ$, and $\beta = 100$ for protons (top panel), and iron nuclei (bottom panel).

eled as a power law with a broken exponential cutoff [15]

$$\frac{dN_{\text{CR},A}}{dt dE} = C_0 \left(\frac{E}{E_0} \right)^{-\gamma} \begin{cases} 1 & E < E_{\text{max}} \\ \exp(1 - E/E_{\text{max}}) & E \geq E_{\text{max}} \end{cases} \quad (9)$$

where C_0 is a normalization constant, γ is the spectral index, and $E_{\text{max}} \equiv E_{\text{max}}(z, M_{\text{vir}}, Z)$ is the maximum energy. Note that the spectral index is the same for all nuclear species considered. The normalization constant C_0 is determined from the CR luminosity which, in turn, is obtained from the accretion rate of clusters. In particular, the kinetic energy per unit time of the accretion shocks at a distance r_{sh} from the cluster center can be written as $\mathcal{L} = f_b G M_{\text{vir}} \langle \dot{M} \rangle / r_{\text{sh}}$ [42], where $f_b = f_0 (M_{\text{vir}}/10^{15} M_\odot)^{0.16}$ [43] is the average baryon fraction in clusters, $r_{\text{sh}} \gtrsim R_{\text{vir}} \simeq 2.6 \times (M_{\text{vir}}/10^{15} M_\odot)^{1/3}$ Mpc [42] is the shock radius and

$$\langle \dot{M} \rangle \simeq 1.01 \times 10^5 \left(\frac{M_{\text{vir}}}{10^{15} M_\odot} \right)^{1.127} (1 + 1.17 z) \mathcal{E}(z) M_\odot \text{ yr}^{-1}, \quad (10)$$

[44] is the mass accretion rate with the function $\mathcal{E}(z) = \sqrt{\Omega_M(1+z)^3 + \Omega_\Lambda}$. In the model, the mass dependence

of f_0 for the cosmology adopted in this work is also considered. In particular, $f_0 = 0.188$ is used for clusters with $M_{500} > 2 \times 10^{14} M_\odot$, whereas for less massive clusters with $M_{500} < 2 \times 10^{14} M_\odot$ we take an average of $f_0 = 0.155$ around the observed scatter (see Ref. [43]).

Therefore, assuming that the CR luminosity is a fraction f_{CR} of the accretion shock kinetic energy rate, the following expression is obtained

$$\mathcal{L}_{\text{CR}}(M_{\text{vir}}, z) = \mathcal{L}_{46} \times 10^{46} \left(\frac{M_{\text{vir}}}{10^{15} M_\odot} \right)^{1.95} (1 + 1.17 z) \mathcal{E}(z) f_{\text{CR}} \text{ erg s}^{-1}, \quad (11)$$

where $\mathcal{L}_{46} = 1.98$ or 1.63 if $f_0 = 0.188$ or 0.155 , respectively. The normalization constant in Eq. (9) is computed assuming that the luminosity corresponding to a nucleus of mass number A is a constant fraction I_A of the total CR luminosity, i.e.

$$\int_{E_{\text{min}}}^{\infty} dE \frac{dN_{\text{CR},A}}{dt dE} E = I_A \mathcal{L}_{\text{CR}}, \quad (12)$$

where E_{min} is the minimum energy of the CRs.

E. The local galaxy cluster sample

The galaxy cluster sample presented in Ref. [45] is adopted to model the distribution of galaxy clusters in the local Universe. This work introduces a sample of the most massive galaxy clusters in our cosmic neighborhood together with a comprehensive, homogeneous list of cluster masses and distances from the Earth. The resulting selection is primarily based on systems from the Planck survey of Sunyaev-Zeldovich (SZ) galaxy clusters [46] which also have an entry in the Tully galaxy groups catalog [47], with some additional clusters selected from various x-ray catalogs (see Ref. [45] and references therein). In total, the cluster catalog comprises a collection of 45 systems within a comoving distance of 227 Mpc from the observer and M_{500} exceeding a mass cutoff of $M_{\text{low}} \sim 2 \times 10^{14} M_\odot$. As noted in Ref. [45], although the selection process is guided by the availability of observational data, the combination of these catalogs should lead to a very complete coverage of massive local clusters. For the selection of local clusters, the SZ mass estimate provided by Ref. [45] is used whenever available. In cases where the latter is not accessible, the x-ray measurement is used. If neither SZ nor x-ray estimates are available, a corrected dynamical mass estimate obtained from the Tully galaxy groups catalog is used. Subsequently, all available M_{500} cluster masses are converted to M_{vir} by assuming an NFW profile and the halo concentrations of Ref. [48]. Using this procedure the condition $M_{500} \gtrsim M_{\text{low}}$ translates into the constraint $M_{\text{vir}} \gtrsim M_{\text{vir,low}}$, with $M_{\text{vir,low}} = 10^{14.57} M_\odot$, which, within uncertainties, is satisfied for about 70% of the systems within 150 Mpc. Additionally, the observed

cluster distances reported in Ref. [45] are considered, except in the cases of Virgo and Fornax where projection effects in the sky introduce systematic errors leading to unreliable distance determinations. Instead, for Virgo, the value given in Ref. [49] is adopted, which conducts a detailed analysis of the distance of about a hundred early type galaxies in the cluster, resulting in a better distance measurement. In the case of Fornax, the recent tip of the giant branch distance measurement provided by Ref. [50] is considered. The list of all massive clusters within 150 Mpc provided by [45] is shown in Table II.

TABLE II. Local sample of massive galaxy clusters within 150 Mpc from Earth sorted by increasing distance according to Ref. [45]. From left to right columns show cluster name/ID, comoving distance, our virial mass estimate (see text) and the observational method used for M_{500} determination.

Name	d [Mpc]	M_{vir} [$10^{14} M_\odot$]	Method
Virgo	$16.70 \pm 0.20^\dagger$	9.16 ± 1.10	SZ
Fornax/AS0373	$19.30 \pm 0.70^\dagger$	$1.77^{+0.62}_{-0.77}$	X
Centaurus/A3526	56.64 ± 27.40	2.26 ± 0.21	SZ
Hydra/A1060	63.30 ± 27.36	$3.49^{+0.89}_{-1.45}$	X
AWM7	70.31 ± 27.31	$7.04^{+1.80}_{-3.30}$	X
Norma/A3627	76.02 ± 25.35	4.80 ± 0.55	SZ
Perseus/A426	78.31 ± 27.31	$8.76^{+2.32}_{-4.21}$	X
A347	82.36 ± 27.33	6.05	dyn
3C129	91.37 ± 26.75	$7.73^{+3.37}_{-3.43}$	X
A3581	103.50 ± 25.27	3.41 ± 0.08	SZ
A1367	103.78 ± 25.27	3.27 ± 0.27	SZ
A2877	105.26 ± 27.22	2.05 ± 0.26	SZ
Coma/A1656	109.30 ± 20.92	10.22 ± 0.40	SZ
A539	129.97 ± 25.26	$3.75^{+0.47}_{-1.23}$	X
A2634	137.52 ± 27.15	$6.43^{+0.99}_{-1.47}$	X
A2197/99	140.23 ± 25.17	5.25 ± 0.25	SZ
A496	150.06 ± 25.16	5.17 ± 0.33	SZ

[†]Refs. [49] and [50].

To approximately reproduce the expected number of clusters in our vicinity, we select all clusters with masses above M_{low} within a comoving distance of 110 Mpc, which for the cosmology adopted in this work corresponds to a redshift of $z_0 = 0.02485$. The resulting sample comprises a total of 8 objects that is consistent at the $\sim 1\sigma$ level (assuming Poissonian uncertainties) with the expected number of massive clusters at $z \leq z_0$ determined by the halo mass function (HMF) of Ref. [51] after a proper scaling to the cosmology adopted in this paper. As a result, the final selection includes some of the most iconic structures present in our cosmic neighborhood such as the Virgo, Hydra, Perseus and Coma galaxy clusters, among others.

It is generally believed that Virgo may account for a significant fraction of the UHECRs arriving at Earth due to its relative proximity (see, e.g., Ref. [24]), compared to other massive but more distant clusters like Perseus or Coma. However, a proper gauging of the relative contribution of the different clusters to the measured CR

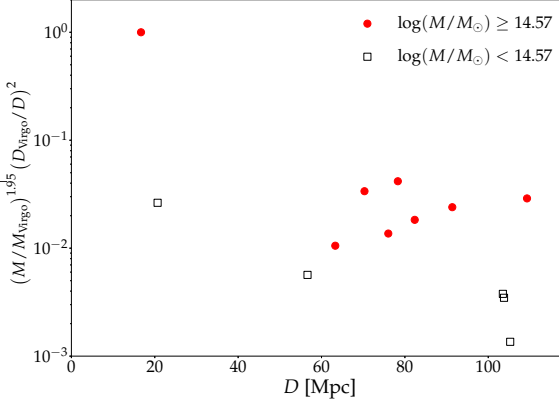


FIG. 3. The weight of each galaxy cluster in the local sample as a function of comoving distance. The masses and distances are normalized to the corresponding values of Virgo. The galaxy clusters are at comoving distances smaller than 110 Mpc.

flux on Earth has to be performed considering cluster masses and distances in a consistent way. Figure 3 shows the weighted contribution of individual clusters in Table II normalized to the corresponding Virgo values as a function of distance. Each cluster is weighted taking into account the mass dependence of the CR luminosity divided by the distance of the cluster squared. This simple calculation indicates that, within this scenario, the Virgo cluster is the dominant CR source, with its weight exceeding that of the rest of the sample by more than an order of magnitude. However, a more rigorous calculation that accounts for both propagation of the different nuclear species and cosmology is ultimately needed, and it will be presented below.

It is worth mentioning that the discrete local cluster sample is approximately complete only for the high-mass

end of the cluster mass distribution within a comoving distance of about 110 Mpc. To take into account the existence of clusters below the mass cutoff imposed in Ref. [45] that may contribute to the overall UHECR flux, the universal, redshift-dependent HMF of Ref. [51] is used to account for clusters with virial masses below the cut-off down to a minimum mass, typical of galaxy groups. In this way, the possibility that galaxy groups in the local Universe also develop an envelope of less-energetic accretion shocks where CRs can accelerate is also considered. As a result, local sources in the model contains a discrete contribution corresponding to well-known, more massive galaxy clusters located in our vicinity, plus a statistical contribution of less-massive systems modeled following the abundance dictated by the HMF evolution in the redshift range $z = [0, z_0]$. Further details of this procedure will be provided in the next section.

III. CHARACTERIZATION OF COSMIC RAY FLUX AND COMPOSITION

A. Flux and composition profile calculation

The propagation of the CRs is affected by their interactions with the low-energy photons of the radiation field that fills the intergalactic medium. The most important photon backgrounds are the CMB and the EBL. The main processes undergone by these particles during propagation are: electron-positron pair photoproduction, pion photoproduction, and photodisintegration of nuclei. Considering a uniform distribution of galaxy clusters, the flux at Earth corresponding to nuclei of mass number A for galaxy clusters located at redshifts between z_a and z_b with virial masses between M_a and M_b (for simplicity, the subscript “vir” will be omitted from the masses in what follows) is given by

$$J_{U,A}(E, z_a, z_b, M_a, M_b) = \frac{c}{4\pi} \sum_{A'} \int_{z_a}^{z_b} dz' \int_{E_{\min}}^{\infty} dE' \int_{M_a}^{M_b} dM \frac{Q_{A'}(E', M, z')}{(1+z') H(z')} \frac{d\bar{n}_{AA'}}{dE}(E; E', z'), \quad (13)$$

where c is the speed of light and $H(z) = H_0 \mathcal{E}(z)$ is the Hubble parameter with its value at $z = 0$ being $H_0 = 67.3 \text{ km s}^{-1} \text{ Mpc}^{-1}$. Here $d\bar{n}_{AA'}(E; E', z')/dE$ is the differential fraction of particles reaching the Earth with energy E and mass number A generated by a nucleus emitted by a galaxy cluster at a redshift z' with energy E' and mass number A' . Also $Q_{A'}$ in Eq. (13) is the number of nuclei with mass number A' injected by the clusters per unit of energy, volume and time, which can be written as

$$Q_{A'}(E', M, z') = \frac{dN_{\text{CR}, A'}}{dt' dE'}(E', z', M) \frac{dn_{\text{CL}}}{dM}(M; z'), \quad (14)$$

where dn_{CL}/dM is the HMF given by Ref. [51].

The distribution $d\bar{n}_{AA'}/dE$ is calculated from Monte Carlo simulations performed by using the CRPropa program [40]. Also, in this case, the EBL model used in the simulations is the one of Ref. [41]. The simulations are performed considering the five different nuclear species mentioned before. CRs are injected in the intergalactic medium at redshift values obtained by sampling a uniform distribution in light-travel distance. Since the fit of the CR data is performed above $10^{18.7} \text{ eV}$ redshift values in the interval $[0, 1]$ are considered [52]. The energy of the injected particles is quantized in discrete steps, each with a width of $\Delta \log(E/\text{eV}) = 0.01$. It ranges from 10^{18} to $Z' \times 10^{21.5} \text{ eV}$, where Z' is the charge number of the injected nuclei.

The flux at Earth from nuclei with mass number A for

$$J_{D,A}(E) = \sum_i \sum_{A'} \frac{1}{(4\pi)^2 r_i^2 (1+z_i)} \int_{E_{\min}}^{\infty} dE' \frac{dN_{\text{CR},A'}}{dt'dE'}(E', z_i, M_i) \frac{d\bar{n}_{AA'}}{dE}(E; E', z_i), \quad (15)$$

where r_i , z_i , and M_i are the comoving distance, the redshift, and the virial mass of the i th cluster of the catalog, respectively. In this case, a set of dedicated simulations are performed in order to calculate $d\bar{n}_{AA'}(E; E', z_i)/dE$ with more statistics. The only difference between these simulations and the previous ones is that, in the latter case, CRs are injected at the positions of each cluster listed in the catalog of Table II.

Since the catalog is obtained for cluster virial masses larger than about $M_{\text{vir,low}}$, the total flux at Earth corresponding to a nucleus of mass number A is given by

$$J_A(E) = J_{D,A}(E) + J_{U,A}(E, z_{\min}, z_{\max}, M_{\min}, M_{\text{vir,low}}) + J_{U,A}(E, z_0, z_{\max}, M_{\text{vir,low}}, M_{\max}), \quad (16)$$

where $z_{\min} = 0$ and $z_{\max} = 1$ are the minimum and maximum redshifts, respectively. For the cluster virial mass range it is assumed that accretion shocks are present from the less-massive galaxy groups to the largest clusters. For M_{\min} two values are considered: 10^{13} and $10^{13.5} M_{\odot}$, which are typical galaxy group mass scales, while $M_{\max} = 10^{16} M_{\odot}$ is taken as an upper limit for the integration. However, due to the HMF distribution, the more massive clusters that contribute significantly to the flux are always less massive than M_{\max} .

The data to be fitted includes the total flux at Earth, the mean value of the natural logarithm of the mass number and its variance, which are given by

$$J(E) = \sum_A J_A(E), \quad (17)$$

$$\langle \ln A \rangle(E) = \frac{\sum_A J_A(E) \ln A}{J(E)}, \quad (18)$$

$$\text{Var}[\ln A](E) = \frac{\sum_A J_A(E) \ln^2 A}{J(E)} - \langle \ln A \rangle(E)^2. \quad (19)$$

B. Fit to experimental data

As mentioned before, the flux and the two first moments of $\ln A$ are fitted considering five nuclear species injected by the sources. The free fitting parameters, γ , f_{CR} and the five luminosity fractions I_A (which are not independent since $\sum_A I_A = 1$) are estimated minimizing a likelihood function, which is composed by three χ^2 terms for the flux and two first moments of $\ln A$ and a Poisson term with $n = 0$ for the two upper limits on the flux reported by Auger at the two highest energy bins

a discrete set of nearby massive clusters is given by

considered. The flux data is taken from Ref. [4], the upper limits on the flux are taken from Ref. [3], and the first two moments of $\ln A$ data are taken from Ref. [6]. Since simulated atmospheric showers are required to obtain the first two moments of $\ln A$ from the X_{\max} parameter, the data generated using the high-energy hadronic interaction models EPOS-LHC [53] and Sibyll 2.3c [54] are considered in this analysis. As mentioned before, the Auger data is fitted above $10^{18.7}$ eV. Since this study focuses on the potential of accretion shocks in galaxy clusters to explain the most energetic CRs, the origin of the ankle lies beyond the scope of this paper. It is important to remark that the Auger directional exposure is not considered in the calculation of the contribution from discrete sources. Instead, it is assumed that the flux measured by Auger accurately reflects the flux that would be observed by an observatory with uniform exposure across the entire sky. While this assumption introduces a limitation to the analysis, the primary goal of this study is to explore the connection between UHECRs and galaxy cluster accretion shocks, rather than to develop a detailed model of the Auger flux and composition measurements. Figure 4 shows the fit of our model to the Auger data for quasiparallel shocks ($\theta = 45^\circ$) in the case of accretion shock model C and high-energy hadronic interaction model EPOS-LHC for $\eta = 1$, $\beta = 100$ and $\log(M_{\min}/M_{\odot}) = 13$. As anticipated, the highest energy portion of the flux is dominated by the contribution of the Virgo cluster, with other nearby galaxy clusters playing a comparatively minor role. Contributions from local Universe clusters with virial masses below $10^{14.57} M_{\odot}$, and those with masses above $10^{14.57} M_{\odot}$ but at redshifts $z = [z_0, 1]$, are only significant well below the flux suppression energy. Crucially, this figure reveals that this model struggles to describe the flux suppression region, which is attributable to the low maximum energies obtained in the scenario under consideration. Conversely, the model successfully fits the composition data. The variance of $\ln A$ between $10^{18.7}$ and $10^{19.2}$ eV is not perfectly reproduced, but the data remain consistent with the model within the total (statistical and systematic) uncertainties. Table III shows the best fit parameters for the case shown in Fig. 4.

The top panel of Fig. 5 presents the best-fit spectral index of the injected spectrum as a function of the angle θ for accretion shock model C with $\log(M_{\min}/M_{\odot}) = 13$. The results are shown for all considered angles and high-energy hadronic interaction models, except for the case of parallel shocks with $\eta = 10$, for which the maximum

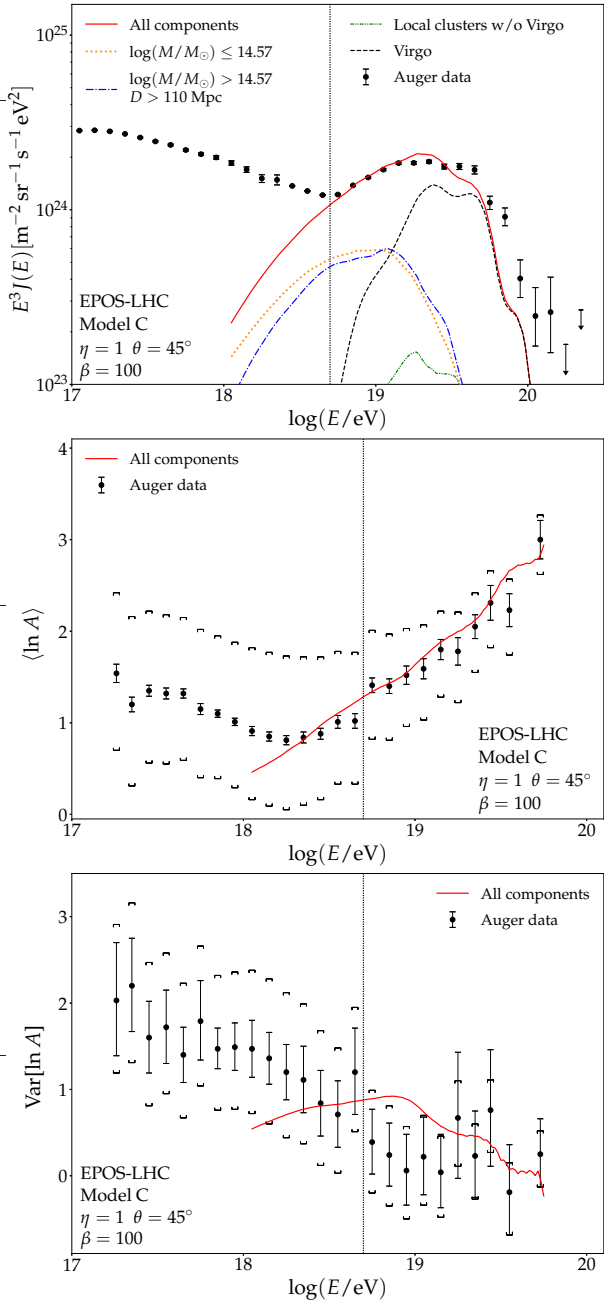


FIG. 4. Top panel: the cosmic ray flux, multiplied by the cube of the energy, as a function of the logarithm of the primary energy. Different cluster contributions to the total flux are shown (see text for details). Middle panel: mean value of $\ln A$ as a function of the logarithm of primary energy. Bottom panel: variance of $\ln A$ as a function of the logarithm of primary energy. In the three plots the data points represent the Auger measurements and the red solid line our best-fit model for $\log(M_{\min}/M_{\odot}) = 13$ and $\beta = 100$. The vertical lines mark the lower energy limit of the data used in the fit. The brackets in the composition data represent the systematic uncertainties.

attainable energies are too low to perform a fit. The figure shows that γ increases with the angle between the magnetic field and the shock normal, generally ranging

TABLE III. Best-fit parameters for the model of Fig. 4.

γ	-1.33 ± 0.05
f_{CR}	$(1.099 \pm 0.004) \times 10^{-2}$
I_{p}	$< 2.7 \times 10^{-6}$
I_{He}	0.54 ± 0.01
I_{N}	0.41 ± 0.01
I_{Si}	0.06 ± 0.02
I_{Fe}	< 0.0069

between -2.2 and 1 . This trend arises because the maximum energy increases with θ , thus requiring larger values of γ to reach higher energies. The resulting γ values further underscore the difficulty in reaching the suppression region of the flux. Notably, γ values obtained for Sibyll 2.3c are larger than those for EPOS-LHC. This difference occurs because Sibyll 2.3c infers a heavier composition, and since heavier primaries attain larger maximum energies, less negative γ values are required for this high-energy hadronic interaction model. The bottom panel of Fig. 5 presents the best-fit values of the CR fraction parameter, f_{CR} , as a function of θ . The plot reveals f_{CR} values of about $0.01 - 0.011$ across different angles. Interestingly, despite the inability of the model to account for the suppression region, these f_{CR} values align with the results obtained in Ref. [23]. Note that, since these models do not reproduce the flux in the suppression region, the corresponding best-fit parameters do not yield an unbiased estimate of the underlying acceleration spectrum. In particular, the fits tend to favor smaller γ values, including negative ones, to compensate for the low maximum energies, thereby biasing the inferred spectral index if UHECRs are indeed accelerated in these types of sources.

The maximum-energy values obtained for models A, B, and C are broadly similar across all primary species, following the ordering $E_{\text{max,C}} > E_{\text{max,A}} > E_{\text{max,B}}$. As a result, only model C and model A with $\eta = 10$ and $\theta = 90^\circ$ for Sibyll2.3c achieve a rough consistency with the suppression region (see Appendix B for model C). In all other scenarios considered, the maximum energies are too low to accurately reproduce the flux suppression. Although the variance of the composition is not perfectly matched in most cases, the overall composition trends remain compatible with the data within total uncertainties. It is important to note that the efficiency of perpendicular shocks in accelerating ions remains an open question (see, however, Ref. [39]). For the models that roughly fit the suppression region, the fitted spectral indexes are 0.96 ± 0.03 for model C and 0.90 ± 0.03 for model A, both corresponding to $\theta = 90^\circ$, $\eta = 10$, and Sibyll2.3c. These results suggest that the inferred values of γ are influenced by the limited maximum energies, the larger spectral index obtained for model C is consistent with its higher maximum energy relative to model A.

While a plasma beta parameter, $\beta = 100$, is consistent with current expectations for galaxy cluster ac-

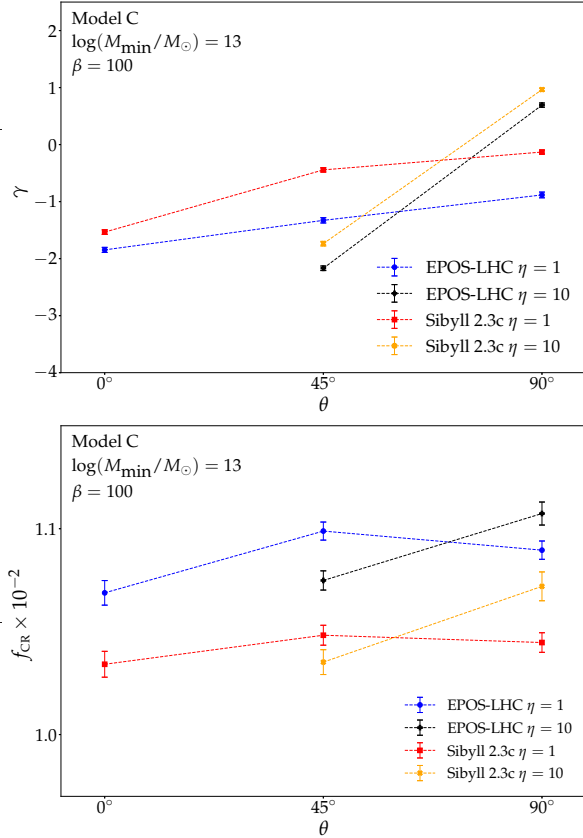


FIG. 5. Spectral index (top panel) and cosmic ray fraction (bottom panel) as a function of θ for all cases under consideration, except $\theta = 0^\circ$ and $\eta = 10$. The minimum value of the galaxy cluster mass considered here is $\log(M_{\min}/M_\odot) = 13$ and $\beta = 100$.

cretion shocks, the equipartition scenario (a frequently adopted assumption in the literature corresponding to $\beta = 1$) is also considered here (see Sec. II A 1). In this case, the maximum energies of the different injected nuclear species become larger, thereby generally allowing for a better fit to experimental data, including the flux. Figure 6 shows the fit of our model to the Auger data for quasiparallel shocks ($\theta = 45^\circ$) in the case of the accretion shock model C and high-energy hadronic interaction model EPOS-LHC for $\eta = 1$, $\beta = 1$ and $\log(M_{\min}/M_\odot) = 13$. As in the previous case, the highest energy portion of the flux is dominated by the contribution of the Virgo cluster. Also, the contribution from local clusters with virial masses below $10^{14.57} M_\odot$, and those with larger masses but at redshifts $z = [z_0, 1]$, are only significant well below the flux suppression energy. The highest energy point of the observed UHECR flux is far from the fitted curve, but its error bar is still quite large and then more statistics is required in that energy bin. The agreement between the best-fit model and the Auger data composition is quite good. Even though the highest-energy data point of the mean value of $\ln A$ appears to deviate from the fit, it remains compatible with it once the total uncertainties are taken into account.

Similar to the $\beta = 100$ case, the data points for the variance of $\ln A$ in the energy range $10^{18.7}$ and $10^{19.2}$ eV are compatible with the fit within total uncertainties. Table IV shows the best fit parameters for the case shown in Fig. 6.

TABLE IV. Best-fit parameters for the model of Fig. 6.

γ	$= 0.91 \pm 0.03$
f_{CR}	$= (1.124 \pm 0.006) \times 10^{-2}$
I_p	$= 0.030 \pm 0.007$
I_{He}	$= 0.39 \pm 0.01$
I_N	$= 0.51 \pm 0.02$
I_{Si}	$= 0.07 \pm 0.01$
I_{Fe}	$< 1.3 \times 10^{-6}$

The top panel of Fig. 7 shows the resulting spectral index of the injected spectrum for the equipartition scenario and accretion shock model C as a function of all considered degrees of freedom (i.e., η , θ and high-energy hadronic interaction model). From the figure, it can be seen that γ increases with θ , roughly taking values between -2 and 1.5 . As in the case of $\beta = 100$, this is due to the fact that the maximum energy increases with the angle between the magnetic field and the shock normal and, then, larger values of γ are required for the spectra in order to reach higher energies. The bottom panel of Fig. 7 shows the best-fit values of the CR fraction parameter, f_{CR} , as a function of θ . It can be seen from the plot that the average value obtained for the different angles is of the order of 0.011 which is, also in this case, consistent with the results obtained in Ref. [23]. It is worth noting that models with $\theta = 0^\circ$, as well as those with $\theta = 45^\circ$ and $\eta = 10$, do not reproduce the flux in the suppression region. Consequently, their best-fit parameters cannot be assigned a meaningful physical interpretation in terms of the underlying accelerated spectrum.

In contrast, models that successfully fit the suppression region yield positive spectral indexes. Scenarios with $\theta = 45^\circ$ and $\eta = 1$ (see Fig. 6 as an example), as well as all models with $\theta = 90^\circ$, can successfully fit the flux, including the suppression region. The spectral indexes of the models that adequately describe the data range from 0.7 to 1.6 , with the highest values corresponding to $\theta = 90^\circ$ and $\eta = 10$. This indicates that models with lower maximum energies have smaller spectral indexes, highlighting their difficulty in reproducing the suppression region. In all cases, the fits to the first two moments of $\ln A$ remain compatible with experimental data within total uncertainties, regardless of whether the suppression region is accurately modeled.

For model D, which assumes a constant $1 \mu\text{G}$ magnetic field across all cluster masses, only the case of $\theta = 90^\circ$ and $\eta = 10$ successfully reproduces the suppression region for both high-energy hadronic interaction models considered. The resulting spectral indexes fitting the data, including the suppression region, are $\gamma = 1.32 \pm 0.03$ and 1.57 ± 0.02 for EPOS-LHC and Sibyll 2.3c, respec-

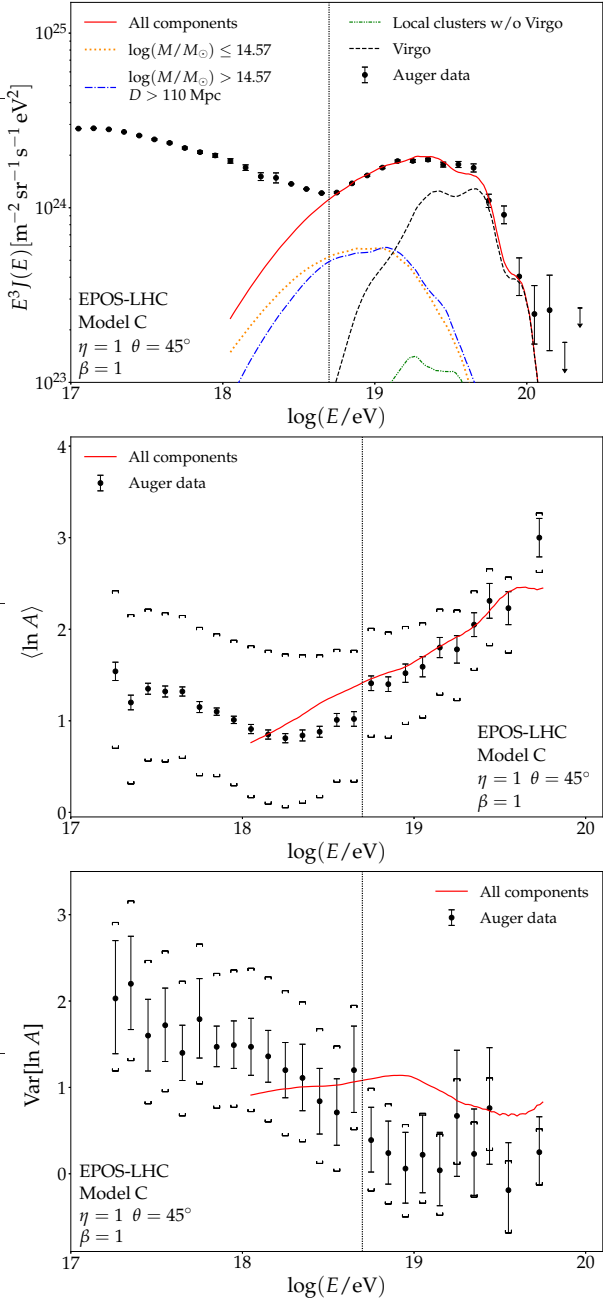


FIG. 6. Top panel: the cosmic ray flux, multiplied by the cube of the energy, as a function of the logarithm of the primary energy. Different cluster contributions to the total flux are shown (see text for details). Middle panel: mean value of $\ln A$ as a function of the logarithm of primary energy. Bottom panel: variance of $\ln A$ as a function of the logarithm of primary energy. In the three plots the data points represent the Auger measurements and the red solid line our best-fit model for $\log(M_{\min}/M_\odot) = 13$ and $\beta = 1$. The vertical lines mark the lower energy limit of the data used in the fit. The brackets in the composition data represent the systematic uncertainties.

tively. As discussed earlier, in these cases the fitted spectral indexes may be interpreted as unbiased estimates of the underlying acceleration spectral index, provided that

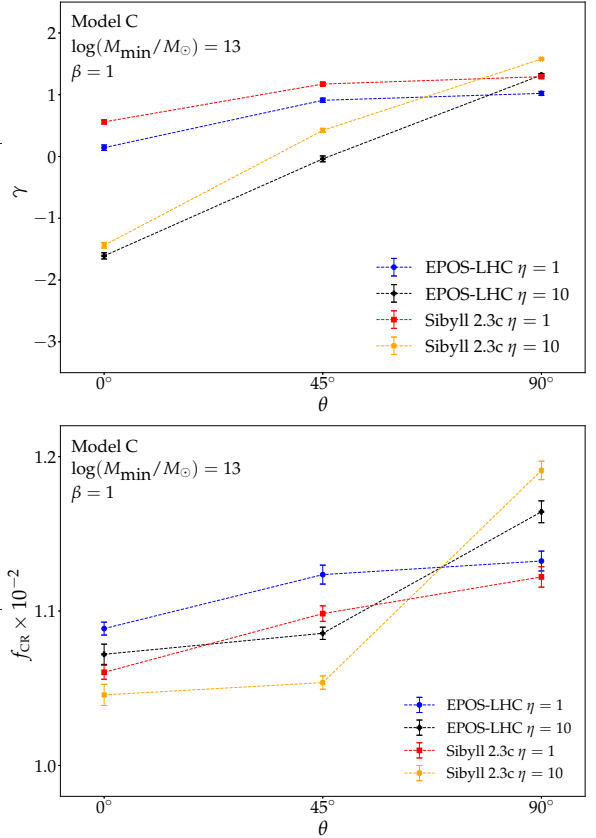


FIG. 7. Spectral index (top panel) and cosmic ray fraction (bottom panel) as a function of θ for all cases under consideration. The minimum value of the galaxy cluster mass considered here is $\log(M_{\min}/M_\odot) = 13$ and $\beta = 1$.

model D is indeed the correct description of the source environment. Note that a scenario with $\eta = 1$ and $\theta = 90^\circ$ also achieves a broad agreement in the suppression region.

Finally, we also investigated the dependence of the fitted parameters on the minimum virial mass of galaxy clusters contributing to the UHECR background. Overall, increasing the minimum considered mass to $\log(M_{\min}/M_\odot) = 13.5$ results in a slight decrease in the low-mass component of the flux. This change has a small impact on the fit performance and on the resulting best-fit values of the model parameters. Consequently, if $\log(M_{\min}/M_\odot) = 13.5$, the resulting fitted γ and f_{CR} values are slightly larger. This is because lower values of the low-mass component require larger values of f_{CR} to fit the flux at low energies. However, since the other components remain unchanged, larger values of γ are needed to also fit the highest-energy part of the spectrum.

IV. DISCUSSION

Cosmological simulations show that θ angles in galaxy cluster accretion shocks can vary considerably [55]. This suggests that the intricate nature of the intracluster

medium ensures the presence of suitable acceleration sites for CR nuclei in external shocks. Note that our accretion shock models are designed to capture global trends at these locations, excluding magnetic field and velocity fluctuations. Therefore, the possibility that small-scale fluctuations along the shock surface could create favorable conditions for ion acceleration is not completely ruled out. In particular, larger magnetic fields can naturally lead to higher maximum energies. However, if particle acceleration is dominated by only a subset of shock patches with favorable conditions for nuclear acceleration, a larger acceleration efficiency, f_{CR} , would be required, since only a fraction of the total kinetic energy flux is processed through those regions.

On the other hand, particle-in-cell simulations modeling the microphysics of CR acceleration show that nuclei are most efficiently accelerated in quasiparallel configurations ($\theta \lesssim 45^\circ$) for strong shocks [56]. However, recent findings show that protons and heavier nuclei might also accelerate in quasiperpendicular shocks [39]. As stated in Refs. [26, 27], preprocessed CR populations at galactic scales might be further reaccelerated in galaxy cluster accretion shocks, which could also promote more efficient acceleration in quasiperpendicular shocks.

For $\beta = 100$, a significant fraction of the considered parameter space is disfavored by current data. Only models A and C (see Table I) with perpendicular shocks and $\eta = 10$, within the context of the Sibyll2.3c hadronic model, can fit the flux including the suppression region. In the equipartition scenario with $\beta = 1$, which is disfavored by current estimates, the UHECR Auger data (both flux and composition) can still be satisfactorily reproduced by models with quasiparallel or perpendicular shocks. In general, in all models that reasonably fit the suppression region, the best-fit values of γ are typically between 0.7 and 1.6 (see Figs. 5 and 7). This contrasts with the $\gamma = 2$ expectation from the first-order Fermi mechanism in the case of strong shocks. Nonetheless, values of $\gamma < 2$, even including negative ones, have also been reported in several analyses (see, e.g., Refs. [15, 52]). This suggests that the fitted spectral index does not necessarily correspond to the intrinsic acceleration index, as CRs may interact with photon and magnetic fields in the acceleration region, modifying the injected spectrum. For accretion shocks in galaxy clusters, an additional population of low-energy photons in the outskirts of the shocks can further modify the acceleration spectrum but the maximum energy can also be affected. Moreover, the magnetic-horizon effect absent in the present work can introduce a low-energy cutoff due to interactions between CRs and the intergalactic magnetic field, and may therefore play an important role. Including this effect in the propagation model can reduce the tension between the fitted γ values and the expectation from the first-order Fermi mechanism, as shown in Ref. [57]. However, the results in Ref. [57] are based on a different cutoff shape, source evolution, and modeling framework. Moreover, the inferred γ may also reflect the spectral index of a hy-

pothetical low-energy component accelerated in the termination shocks of powerful galaxies and subsequently reaccelerated in cluster external shocks [26, 27]. In any case, the fact that the spectral indexes obtained from fits to Auger data are smaller than those expected from the first-order Fermi mechanism remains as an open problem in UHECR physics.

The results obtained for $\beta = 100$ suggest a scenario in which the observed UHECR flux could be composed of a galaxy cluster component that dominates at lower energies, together with the contribution of one or a few of other local sources—potentially including the radio galaxy Centaurus A—which dominate the flux in the suppression region. In such a scenario, it is possible to explore more realistic values of γ corresponding to the cluster component, since the physical meaning of a parameter in a given model can only be assessed when the model is capable of fully reproducing the experimental data. A model of this type will be developed in future studies.

The best-fit values of the CR fraction parameter, f_{CR} , are of order 0.01 for all models considered, regardless of whether they successfully reproduce the suppression region of the flux. This occurs because the fit to f_{CR} depends solely on the flux normalization and is therefore dominated by the flux level at the minimum energy considered, where the experimental uncertainties are small. As previously noted, this value is consistent with the estimate reported in Ref. [23], although that analysis adopted a spectral index of 1.7, which differs significantly from several of the values obtained in this work. Moreover, among the models compatible with the experimental data, the minimum γ value we found is approximately 0.7. Thus, even if the derived f_{CR} values are consistent with those reported in Ref. [23], the corresponding accelerated spectra may differ significantly, because models with harder spectra inject substantially more particles at high energies, and fewer at lower energies, than models with softer spectra at the same luminosity.

As mentioned before, the highest-energy part of the UHECR flux is dominated by the contribution from Virgo. However, neither the Auger nor the TA data shows any excess in the Virgo region (see Sec. I). This fact could be explained either by the inability of cluster accretion shocks to accelerate UHECRs or, even if UHECR acceleration is efficient, by the action of different mechanisms, often involving magnetic deflections. In particular, some alternatives have been proposed in this respect. In the model of Ref. [58], CRs from the Virgo cluster are able to escape through magnetized filaments before being scattered toward the Earth. This model has been developed to explain the TA hotspot, which is located far from the direction of Virgo. Additionally, the Galactic magnetic field can play a significant role. In particular, in Ref. [59] it is shown that strong magnetic demagnification could explain the absence of CR flux excess in this region of the sky.

V. CONCLUSIONS

In this work, we studied the possibility that UHECRs are accelerated in external accretion shocks present in galaxy clusters. We modeled the contribution of nearby massive clusters, including Virgo, as a discrete set, while the remaining sources were assumed to follow a continuous distribution given by the number density of cluster halos which, in turn, is determined by the redshift-dependent HMF. Assuming that sources inject multiple nuclear species with a spectrum following a power law with an exponential cutoff, we performed fits both for the flux at Earth and the composition profile measured by the Pierre Auger Observatory. We found that the flux at the highest energies is dominated by Virgo, while the contribution of the remaining nearby clusters is less significant, mainly involving smaller energies.

After considering a series of accretion shock models with plasma beta parameter $\beta = 100$ (see Table I), i.e. consistent with expectations in galaxy cluster outskirts, we found that all models with $\theta \sim 45^\circ$ can reasonably reproduce both the mean and variance of the CR composition within total uncertainties. However, they do not properly fit the ultrahigh-energy suppression of the CR flux, thus failing to reproduce the highest-energy UHECRs that originate from direct acceleration of thermal particles. Only some models with $\eta = 10$ and $\theta = 90^\circ$ can additionally fit the flux in the suppression region. This suggests that additional, prior reacceleration may be necessary to reproduce the data within the framework of these accretion shock scenarios. For accretion shock models with $\beta = 1$, which are disfavored by current theoretical expectations, the resulting magnetic fields at the shock locations are roughly an order of magnitude stronger than in the $\beta = 100$ case. Consequently, both the composition and flux of the UHECR spectrum can also be reasonably reproduced, within uncertainties.

The best-fit spectral indexes for the models that successfully describe the experimental data lie between approximately 0.7 and 1.6, in agreement with other analyses based on Pierre Auger Observatory data. Concerning the fraction of kinetic energy of the infalling material that must be converted into CRs, we find that all models consistent with the data require efficiencies of a few percent, also compatible with previous results.

The absence of an excess in the CR distribution toward the direction of Virgo may be attributed either to the inability of accretion shocks to accelerate nuclei to the highest observed energies or, potentially, for scenarios reproducing the suppression region, to the interaction of the accelerated CRs with the magnetic fields of the filaments connected to Virgo, and/or to their deflection within the Galactic magnetic field.

Finally, based on our results, we conclude that accretion shocks in galaxy clusters can contribute significantly to the origin of the most energetic UHECRs only if magnetic fields are stronger than typically expected in these environments, which could arise from the existence of lo-

cal fluctuations in the shock front properties, or in the case of perpendicular shock normal-magnetic field configurations. This scenario, however, may also account for all or part of the observed flux at intermediate energies.

ACKNOWLEDGMENTS

A.D.S. and S.E.N. are members of the Carrera del Investigador Científico of CONICET, Argentina. They acknowledge support from CONICET (PIBAA R73734 and PIP 11220200102979CO). S. E. N. also acknowledges support from Agencia Nacional de Promoción Científica y Tecnológica (PICT 2021-GRF-TI-00290).

VI. DATA AVAILABILITY

The data that support the findings of this article are not publicly available. The data are available from the authors upon reasonable request.

Appendix A: CONTRIBUTION OF DIFFERENT PROCESSES TO THE TOTAL MEAN FREE PATH

As mentioned in Sec. II C, the processes included in the interaction time calculation are: photo-pion production, photo-disintegration, and pair production. The energy loss due to the adiabatic expansion of the Universe is also considered. Figure 8 shows the logarithm of the mean interaction time of proton and iron nuclei as a function of the logarithm of energy including the contribution of each individual process to the total interaction time. The photon fields considered are the CMB and the EBL. The EBL model used in the calculations is that of Ref. [41].

Appendix B: FIT TO ACCRETION SHOCK MODEL C

Figure 9 presents the fit of both the flux and composition data for the accretion shock model C with $\beta = 100$ for perpendicular shocks, $\eta = 10$, and Sibyll2.1c as the high-energy hadronic interaction model. This model provides a reasonable fit to the composition data and can better reproduce the suppression region of the flux. Additionally, Table V shows the corresponding best-fit parameters. Note that similar results are obtained for the accretion shock model A with $\beta = 100$ for perpendicular shocks, $\eta = 10$, and Sibyll2.1c.

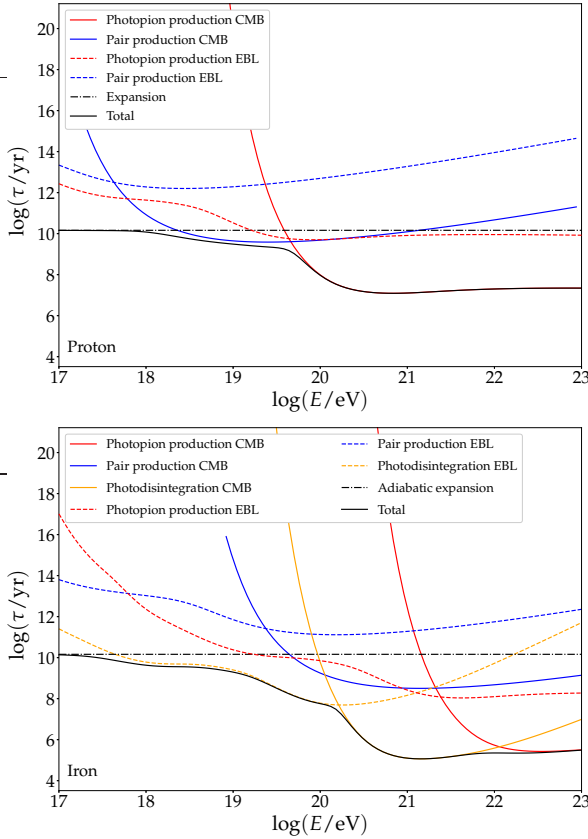


FIG. 8. Logarithm of the mean interaction time as a function of the logarithm of energy for protons (top panel) and iron nuclei (bottom panel) at redshift zero.

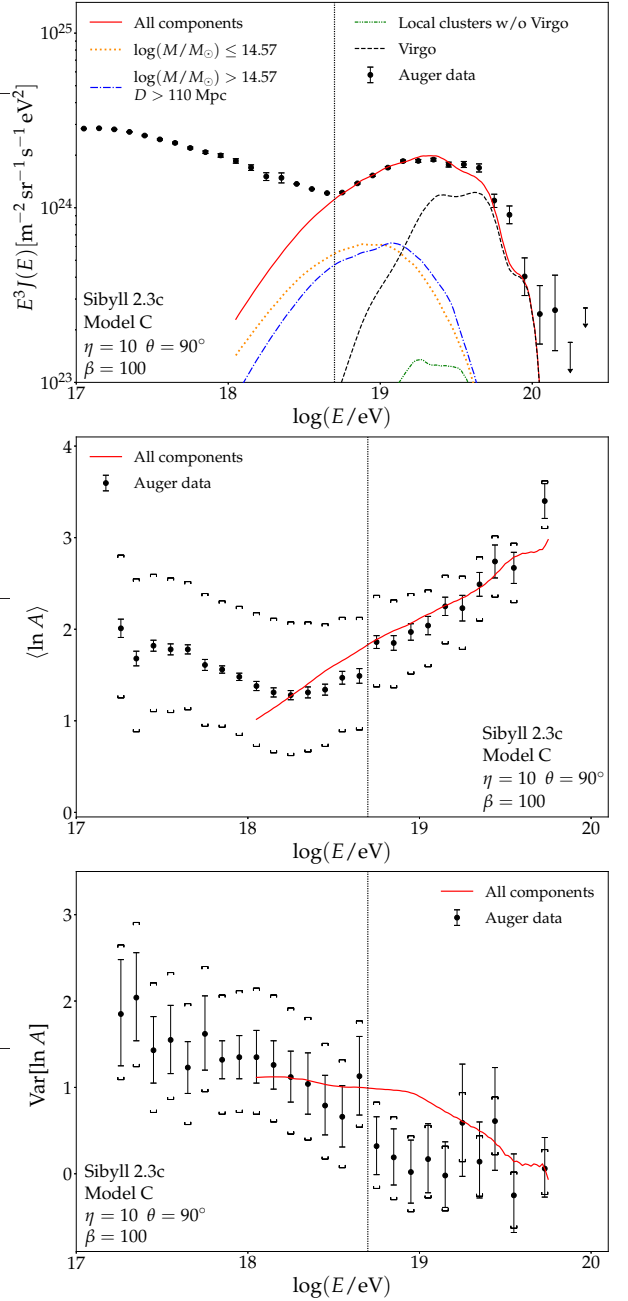


FIG. 9. Top panel: the cosmic ray flux, multiplied by the cube of the energy, as a function of the logarithm of the primary energy. Different cluster contributions to the total flux are shown. Middle panel: mean value of $\ln A$ as a function of the logarithm of primary energy. Bottom panel: variance of $\ln A$ as a function of the logarithm of primary energy. In the three plots the data points represent the Auger measurements and the red solid line our best-fit model for $\log(M_{\min}/M_{\odot}) = 13$ and $\beta = 100$. The vertical lines mark the lower energy limit of the data used in the fit. The brackets in the composition data represent the systematic uncertainties.

TABLE V. Best-fit parameters for the model of Fig. 9.

γ	$= 1.57 \pm 0.02$
f_{CR}	$= (1.072 \pm 0.007) \times 10^{-2}$
I_p	$< 2 \times 10^{-6}$
I_{He}	$= 0.21 \pm 0.02$
I_{N}	$= 0.62 \pm 0.02$
I_{Si}	$= 0.15 \pm 0.01$
I_{Fe}	$= 0.02 \pm 0.01$

[1] A. Aab *et al.* (Pierre Auger Collaboration), Nucl. Instrum. Methods Phys. Res., Sect. A **798**, 172 (2015).

[2] H. Kawai *et al.* (Telescope Array Collaboration), Nucl. Phys. B, Proc. Suppl. **175-176**, 221 (2008).

[3] A. Aab *et al.* (Pierre Auger Collaboration), Phys. Rev. D **102**, 062005 (2020).

[4] P. Abreu *et al.* (Pierre Auger Collaboration), Eur. Phys. J. C **81**, 966 (2021).

[5] A. D. Supanitsky, Galaxies **10**, 75 (2022).

[6] A. Yushkov *et al.* (Pierre Auger Collaboration), Proc. Sci. ICRC2019, 482 (2019).

[7] E. W. Mayotte *et al.* (Pierre Auger Collaboration), Proc. Sci. ICRC2023, 365 (2023).

[8] A. Abdul Halim *et al.* (Pierre Auger Collaboration), Phys. Rev. Lett. **134**, 021001 (2025).

[9] A. Abdul Halim *et al.* (Pierre Auger Collaboration), Phys. Rev. D **111**, 022003 (2025).

[10] A. Abdul *et al.* (Pierre Auger Collaboration), Proc. Sci. ICRC2023, 252 (2023).

[11] A. Aab *et al.* (Pierre Auger Collaboration), Science **357**, 1266 (2017).

[12] J. Kim *et al.* (Telescope Array Collaboration), Proc. Sci. ICRC2023, 244 (2023).

[13] R. Aloisio, V. Berezinsky, and P. Blasi, J. Cosmol. Astropart. Phys. **10** (2014), 020.

[14] S. Mollerach and E. Roulet, Phys. Rev. D **101**, 103024 (2020).

[15] A. Abdul Halim *et al.* (Pierre Auger Collaboration), J. Cosmol. Astropart. Phys. **05** (2023), 024.

[16] M. Unger, G. R. Farrar, and L. A. Anchordoqui, Phys. Rev. D **92**, 123001 (2015).

[17] N. Globus, D. Allard, R. Mochkovitch, and E. Parizot, Mon. Not. R. Astron. Soc. **451**, 751 (2015).

[18] N. Globus, D. Allard, and E. Parizot, Phys. Rev. D **92**, 021302 (2015).

[19] M. Kachelrieß, O. Kalashev, S. Ostapchenko, and D. V. Semikoz, Phys. Rev. D **96**, 083006 (2017).

[20] K. Fang and K. Murase, Nat. Phys. **14**, 396 (2018).

[21] A. D. Supanitsky, A. Cobos, and A. Etchegoyen, Phys. Rev. D **98**, 103016 (2018).

[22] H. Kang, J. P. Rachen, and P. L. Biermann, Mon. Not. R. Astron. Soc. **286**, 257 (1997).

[23] S. Inoue, G. Sigl, F. Miniati, and E. Armengaud, arXiv:astro-ph/0701167.

[24] V. N. Zirakashvili and V. S. Ptuskin, J. Phys. Conf. Ser. **1181**, 012033 (2019).

[25] P. Simeon, N. Globus, K. S. S. Barrow, and R. Blandford, Proc. Sci. ICRC2023, 369 (2023).

[26] R. D. Blandford, P. Simeon, N. Globus, P. Mukhopadhyay, E. Peretti, K. S. S. Barrow, and C. Kim, Proc. Sci. ICRC2023, 127 (2023).

[27] P. Simeon, N. Globus, K. S. S. Barrow, and R. Blandford, arXiv:2503.10795.

[28] Q. Li, W. Cui, X. Yang, R. Davé, E. Rasia, S. Borgani, M. Massimo, A. Knebe, K. Dolag, and J. Sayers, Mon. Not. R. Astron. Soc. **523**, 1228 (2023).

[29] P. A. R. Ade *et al.* (Planck Collaboration), Astron. Astrophys. **571**, A16 (2014).

[30] G. L. Bryan and M. L. Norman, Astrophys. J. **495**, 80 (1998).

[31] M. Arnaud, G. W. Pratt, R. Piffaretti, H. Böhringer, J. H. Croston, and E. Pointecouteau, Astron. Astrophys. **517**, A92 (2010).

[32] H. Böhringer *et al.*, Astron. Astrophys. **469**, 363 (2007).

[33] A. M. Rost *et al.*, Mon. Not. R. Astron. Soc. **527**, 1301 (2024).

[34] L. D. Landau and E. M. Lifshitz, *Fluid Mechanics*, 1st ed., Course of Theoretical Physics, Vol. 6 (Pergamon Press, London, Paris, Frankfurt, 1959).

[35] J.-H. Ha, D. Ryu, and H. Kang, Astrophys. J. **943**, 119 (2023).

[36] C. Loken, M. L. Norman, E. Nelson, J. Burns, G. L. Bryan, and P. Motl, Astrophys. J. **579**, 571 (2002).

[37] J. R. Jokipii, Astrophys. J. **313**, 842 (1987).

[38] D. Allard and R. J. Protheroe, Astron. Astrophys. **502**, 803 (2009).

[39] L. Orusa and D. Caprioli, Phys. Rev. Lett. **131**, 095201 (2023).

[40] R. Alves Batista *et al.*, J. Cosmol. Astropart. Phys. **09** (2022), 035.

[41] R. C. Gilmore, R. S. Somerville, J. R. Primack, and A. Domínguez, Mon. Not. R. Astron. Soc. **422**, 3189 (2012).

[42] K. Fang and A. V. Olinto, Astrophys. J. **828**, 37 (2016).

[43] A. H. Gonzalez, S. Sivanandam, A. I. Zabludoff, and D. Zaritsky, Astrophys. J. **778**, 14 (2013).

[44] J. McBride, O. Fakhouri, and C.-P. Ma, Mon. Not. R. Astron. Soc. **398**, 1858 (2009).

[45] E. Hernández-Martínez, K. Dolag, B. Seidel, J. G. Sorce, N. Aghanim, S. Pilipenko, S. Gottloeber, T. Lebeau, and M. Valentini, Astron. Astrophys. **687**, A253 (2024).

[46] P. A. R. Ade *et al.* (Planck Collaboration), Astron. Astrophys. **571**, A29 (2014).

[47] R. B. Tully, Astrophys. J. **149**, 171 (2015).

[48] A. R. Duffy, J. Schaye, S. T. Kay, and C. Dalla Vecchia, Mon. Not. R. Astron. Soc. **390**, L64 (2008).

[49] S. Mei, J. P. Blakeslee, P. Côté, J. L. Tonry, M. J. West, L. Ferrarese, A. Jordán, E. W. Peng, A. Anthony, and D. Merritt, Astrophys. J. **655**, 144 (2007).

[50] G. S. Anand, R. B. Tully, Y. Cohen, D. I. Makarov, L. N. Makarova, J. B. Jensen, J. P. Blakeslee, M. Cantiello, E. Kourkchi, and G. Raimondo, Astrophys. J. **973**, 83 (2024).

[51] J. Tinker, A. V. Kravtsov, A. Klypin, K. Abazajian, M. Warren, G. Yepes, S. Gottlöber, and D. E. Holz, Astrophys. J. **688**, 709 (2008).

[52] A. Aab *et al.* (Pierre Auger Collaboration), J. Cosmol. Astropart. Phys. **04** (2017), 038.

[53] T. Pierog, I. Karpenko, J. M. Katzy, E. Yatsenko, and K. Werner, Phys. Rev. C **92**, 034906 (2015).

[54] F. Riehn, R. Engel, A. Fedynitch, T. K. Gaisser, and T. Stanev, EPJ Web Conf. **208**, 11002 (2019).

[55] S. Banfi, F. Vazza, and D. Wittor, Mon. Not. R. Astron. Soc. **496**, 3648 (2020).

[56] D. Caprioli and A. Spitkovsky, Astrophys. J. **783**, 91 (2014).

[57] A. Abdul Halim *et al.* (Pierre Auger Collaboration), J. Cosmol. Astropart. Phys. **07**, 094 (2024).

[58] J. Kim, D. Ryu, H. Kang, S. Kim, and S.-C. Rey, Sci. Adv. **5**, eaau8227 (2019).

[59] D. Allard, J. Aublin, B. Baret, and E. Parizot, *Astron. Astrophys.* **686**, A292 (2024).